

Nonreciprocal nonlocal spin transport observed in Dirac semimetal Cd₃As₂ nanoplates

An-Qi Wang,¹ Peng-Zhan Xiang,¹ and Zhi-Min Liao^{1,2,*}

¹State Key Laboratory for Mesoscopic Physics and Frontiers Science Center for Nano-optoelectronics, School of Physics, Peking University, Beijing 100871, China

²Hefei National Laboratory, Hefei 230088, China



(Received 29 March 2022; revised 9 March 2023; accepted 13 April 2023; published 27 April 2023)

Nonreciprocal transport phenomena, such as current direction dependent resistance, have recently attracted substantial research interest due to the underlying physics and potential applications for high-performance rectifiers. Here we report the observation of nonreciprocal spin transport in Dirac semimetal Cd₃As₂ nanoplates under nonlocal configuration. Nonlocal spin voltage amplitude exhibits an anomalous nonreciprocity with respect to the direction of local bias current. It is found that the nonreciprocity is prominent in the region near current leads and becomes more significant upon increasing the bias current amplitude and tuning the Fermi level toward the Dirac point. This unusual nonreciprocity can be well understood by combining the charge current spreading and thermally induced spin polarization of topological surface states. Our results reveal the influence of thermal effect on the spin transport of topological surface states in nonlocal configuration, which should be valuable for thermal spintronics based on topological materials.

DOI: [10.1103/PhysRevB.107.165423](https://doi.org/10.1103/PhysRevB.107.165423)

I. INTRODUCTION

Three-dimensional topological semimetals are believed to possess topological surface and hinge states [1–9], both of which possess a helical spin texture [10–13]. Under an electric current bias, the spin texture of topological states leads to spin-polarized currents with the spin polarization locked to the electron momentum [4,5]. This makes it possible to control the spin polarization by electric means. Furthermore, these topological states are robust against environmental perturbations (e.g., disorders and temperature lifting) and inherit a much longer mean free path [9,14,15], showing great potential for low-dissipation spintronic applications [16]. Current-induced spin polarization has been widely investigated in topological semimetal materials [14,15,17–22]. For example, the Dirac semimetal Cd₃As₂ demonstrates a much higher spin-polarization rate than that in topological insulators [14,15,17]. In addition, current-induced perpendicular magnetization switching has been demonstrated in nanostructured Weyl semimetal WTe₂/ferromagnet heterojunctions [21,23].

Despite the above-mentioned progress achieved so far, certain obstacles still hinder the applications of spintronic devices based on topological semimetals. The existence of conductive bulk channels reduces the contribution of topological states to conductance and thus decreases the charge-to-spin conversion efficiency. Additionally, in the presence of a charge current, the bulk may possibly give rise to spin polarization on the sample surface via the spin Hall effect [18,24,25] and Rashba spin splitting states [15,25,26]. Thus, for achieving highly spin-polarized electron transport,

it is necessary to suppress and even eliminate the bulk contribution. Nonlocal measurements offer a method to single out the topologically protected spin transport [14,27–31]. In the nonlocal region, the contribution of Ohmic current leakage vanishes exponentially [32,33], thus greatly suppressing the transport from bulk states. By contrast, the large mean free path of the topological surface and hinge states results in the current spreading nonlocally away from the region between source and drain electrodes [31,34–37].

In this work, we investigate spin-polarized transport in Dirac semimetal Cd₃As₂ nanoplates under nonlocal configuration. Ferromagnetic Co electrodes are used for spin-dependent voltage measurements. Driven by nonlocal spreading currents, magnetic hysteretic loops of spin voltage are observed in the nonlocal region away from the source-drain region. The nonlocal spin voltage amplitude exhibits a strong dependence on the bias current direction, that is, a nonreciprocal spin transport. This nonreciprocity is enhanced when the sample Fermi level is tuned to near the Dirac point. The results are well understood by the combination of current spreading and thermal effect induced spin polarization of topological surface states.

II. METHODS

Cd₃As₂ nanoplates were obtained via the chemical vapor deposition method [15,17] with a thickness of ~100 nm, and then transferred onto the Si substrate with a 285-nm-thick SiO₂ layer on top. The SiO₂/Si substrate acts as the back gate to modulate the carrier density and Fermi level of the nanoplate. Two rounds of *e*-beam lithography were utilized to pattern the Ti/Au (5 nm/150 nm) and Co/Au (150 nm/10 nm) electrodes. For establishing Ohmic contact between the nanoplate and Ti/Au electrodes, an *in situ* Ar⁺ etching

*liaozm@pku.edu.cn

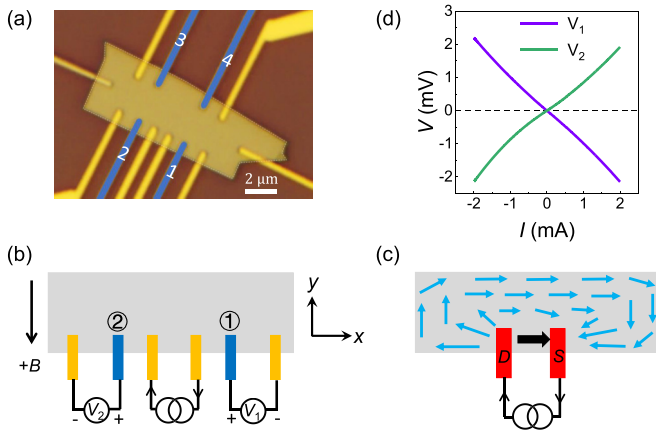


FIG. 1. Nonlocal transport measurements of the Cd_3As_2 nanoplate. (a) Optical image of the nanoplate device A. The Ti/Au and Co electrodes are marked by yellow and blue, respectively. The Co electrodes denoted by 1–4 are mainly used for measurements. (b) Schematic illustration of nonlocal measurements. The nonlocal voltage measured on Co electrodes 1 and 2 is denoted by V_1 and V_2 , respectively. The positive current is applied along the $+x$ direction, and the positive magnetic field is applied along the $-y$ direction. (c) Distribution of the current flow in the nanoplate. The local current channel between the source (S) and drain (D) is denoted by the black arrow, and the nonlocal transport is denoted by the bright blue arrows. Here, the nanoplate is n -type doped and electrons are the majority carriers. (d) Nonlocal I - V characteristics measured using the Co electrodes 1 and 2 in device A, respectively, without applying magnetic field.

treatment was performed before metal evaporation. An upper gold layer was used to protect the Co from oxidation. Several devices were fabricated and measured, showing consistent experimental results. In the following, we will mainly discuss two typical devices, denoted as device A and device B (see Appendix A). Figure 1(a) shows the optical image of device A, where electrodes are placed along the periphery of the nanoplate for nonlocal measurements. All the transport measurements were carried out at a temperature of 1.5 K.

III. RESULTS AND DISCUSSION

As shown in Fig. 1(b), a dc bias current is injected into the nanoplate via the middle two Ti/Au electrodes, whereas the spin-dependent voltage V_S is measured using the Co electrodes 1 and 2 outside the source-drain region, respectively. The V_S is dependent on the relative orientation of magnetization M of the Co electrode and the electron spin polarization S . Specifically, $M//S$ and $M//\bar{S}$ lead to high- and low-voltage states [26,38], respectively. An external magnetic field B is applied along the y axis to modulate the Co electrode magnetization M . All the V_S data in this work are obtained after subtracting the background.

For the Dirac semimetal Cd_3As_2 , bulk, surface, and hinge states are in parallel conduction to carry the current transport. The bulk-state currents dominate between the source and drain. In the region away from the source and drain, the bulk contribution is gradually decreased, and topological surface states and hinge states become manifest due

to their topological protection and longer mean free path [3,8,9,14,15], leading to nonlocal transport [blue arrows in Fig. 1(c)]. Figure 1(d) presents the nonlocal current-voltage (I - V) characteristics measured using the Co electrodes 1 and 2. The slopes of two I - V traces are consistent with the direction of nonlocal current flow depicted in Fig. 1(c). A small deviation away from the linear I - V dependence is observed at high current bias (see Appendix B), which may arise from the thermal effect [39,40].

Figure 2 shows the nonlocal spin transport results measured using the Co electrodes 1 and 2, which are close to the source-drain leads [see the measurement configuration in Fig. 1(b)]. As shown in Figs. 2(a) and 2(b), under a bias current $I = 2$ mA, magnetic hysteric loops of V_S are clearly observed (see the raw data in Appendix C). The spin polarization S can be obtained according to the spin voltage V_S and the Co electrode magnetization M . The nonlocal electron momentum k_e is oriented along the $+x$ direction [Fig. 1(c)]. With the determined orientations of S and k_e , it is found that S is always locked to k_e by the right-handed way, as shown by the insets in Figs. 2(a) and 2(b). Upon reversing the bias current direction [Figs. 2(c) and 2(d)], the spin-polarization orientation is also inverted due to the spin-momentum locking property [14,15,17]. However, notably, the V_S loop height experiences an obvious change upon reversing the current direction, in striking contrast to the spin transport results reported previously [14,15,17,26,37,41–44]. We define the magnetic hysteresis window height as $|\Delta V_S|$, which can be used to characterize the spin voltage amplitude. Figures 2(e) and 2(f) show the current dependence of $|\Delta V_S|$. It is found that $|\Delta V_S|$ is asymmetric with respect to the direction of bias current, and this asymmetry becomes more prominent with higher current bias.

We further investigate the gate voltage dependence of nonreciprocal spin signals in nonlocal geometry. The local transfer curve [Fig. 3(a)] indicates the studied nanoplate is heavily electron doped, where the Dirac point is located around -60 V. Figures 3(b) and 3(c) display the gate voltage V_g dependence of spin signals $|\Delta V_{1S}|$ and $|\Delta V_{2S}|$, respectively. Both $|\Delta V_{1S}|$ and $|\Delta V_{2S}|$ exhibit an increasing trend as the Fermi level is tuned toward the Dirac point, regardless of the direction of bias current (see Appendix D). This can be understood since the bulk conduction is decreased near the Dirac point [14,15,17], whereas the helical surface and hinge states become manifest. In addition, it is found that the spin signal is nonreciprocal with respect to the current direction in the entire gate voltage modulation range. $|\Delta V_{1S}|$ is always larger at $I = -2$ mA than at $I = 2$ mA, while $|\Delta V_{2S}|$ exhibits a much larger value at 2 mA than at -2 mA. The difference of spin signals between $I = 2$ and -2 mA, i.e., $|\Delta V_{1S}|_+ - |\Delta V_{1S}|_-$, is plotted versus V_g , as shown in Fig. 3(d). When tuning V_g from 30 to -60 V, the absolute value of $|\Delta V_{1S}|_+ - |\Delta V_{1S}|_-$ exhibits an increase by a factor of ~ 1.4 , analogous to the increase of local resistance by a factor of 1.5 [Fig. 3(a)]. This implies that the asymmetric effect may be associated with the electrical resistance between the source and drain electrodes.

Besides the region adjacent to source-drain leads, we also study the spin transport in the region far away from the source and drain. As sketched in Fig. 4(a), a dc current is applied on one side of the nanoplate, while the voltage is measured on

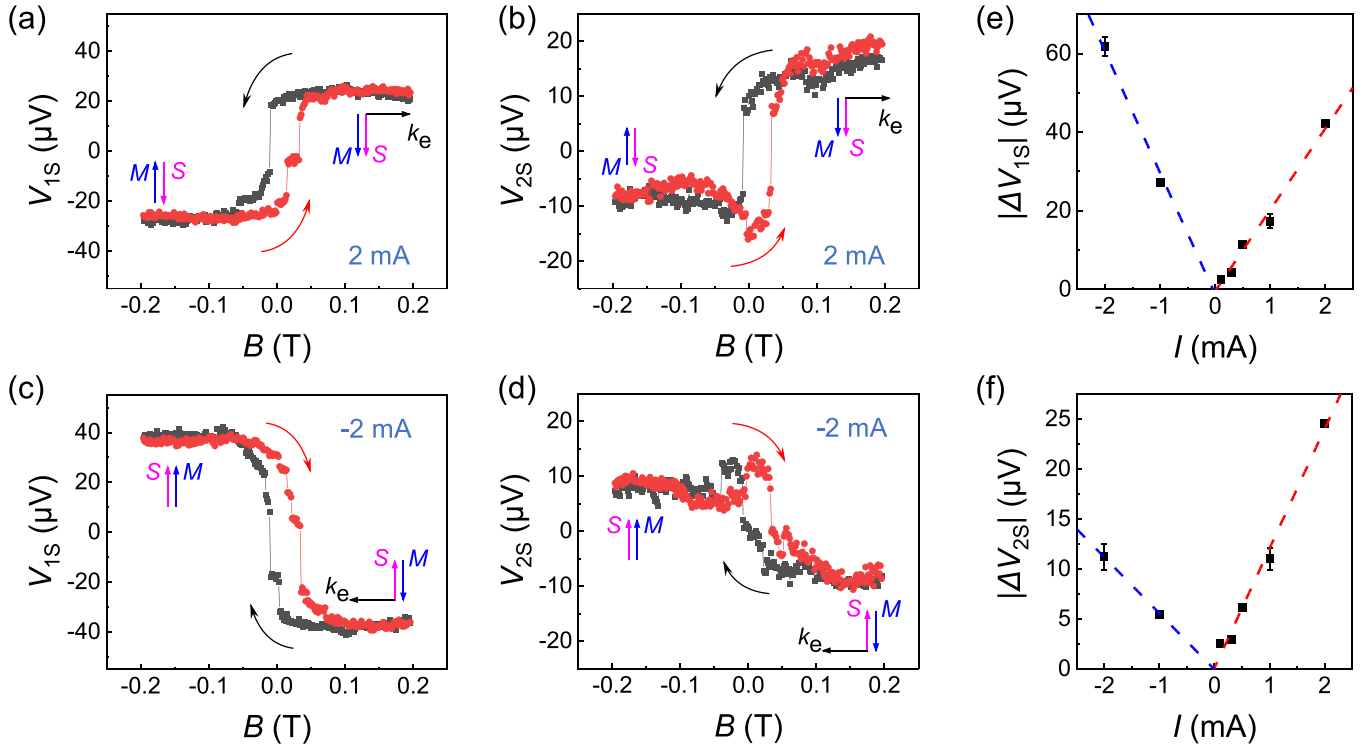


FIG. 2. Nonreciprocal nonlocal spin transport in device A. (a–d) Nonlocal spin voltage V_S loops measured on the Co electrodes 1 and 2 with bias current $\pm 2\text{ mA}$. Insets show the corresponding spin-momentum locking, where the nonlocal electron spin and momentum are denoted by magenta and black arrows, respectively. The V_S is obtained after the background subtraction. Red and black arrows denote the forward and backward sweeping of the magnetic field, respectively. (e, f) Spin voltage amplitude $|\Delta V_{1S}|$ and $|\Delta V_{2S}|$ as a function of bias current I . A nonreciprocity of $|\Delta V_S|$ is observed with respect to the current direction. Dashed blue and red lines are linear fits to experimental data at negative and positive currents, respectively. The error bars represent the standard deviation over multiple measurements.

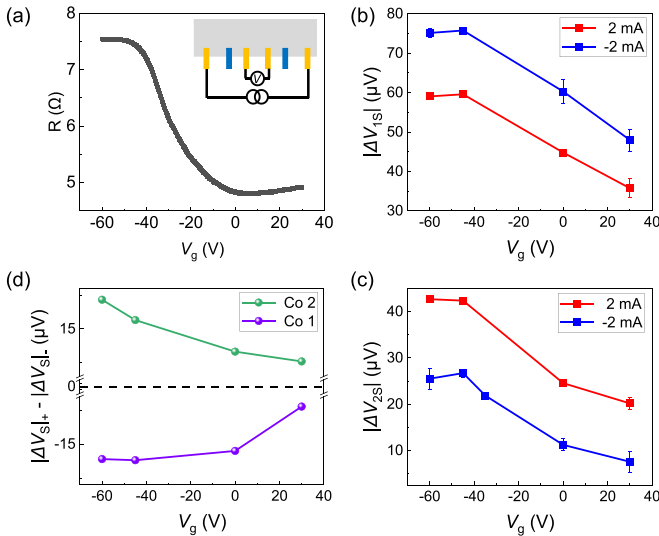


FIG. 3. Gate voltage dependence of nonlocal spin transport in device A. (a) The transfer curve of the nanoplate, obtained from the local four-probe measurement (as schematized in the inset). (b, c) Gate voltage dependence of the nonlocal spin voltage amplitude $|\Delta V_{1S}|$ and $|\Delta V_{2S}|$ with bias current $\pm 2\text{ mA}$. The error bars represent the standard deviation over multiple measurements. (d) The difference of $|\Delta V_S|_+$ and $|\Delta V_S|_-$ versus gate voltage V_g measured on the Co electrodes 1 and 2, respectively. $|\Delta V_S|_+$ and $|\Delta V_S|_-$ correspond to the $|\Delta V_S|$ under $I = 2$ and -2 mA , respectively.

the Co electrodes 3 and 4 situated at the opposite side. Spin voltage loops are also observed here with the spin orientation locked at a right angle to the momentum (see Appendix E). Figures 4(b) and 4(c) show the current dependence of $|\Delta V_{3S}|$ and $|\Delta V_{4S}|$, respectively. It is found that the spin voltage amplitude $|\Delta V_{3S}|$ ($|\Delta V_{4S}|$) stays nearly equivalent under the same magnitude of positive and negative currents, even if the bias reaches up to $\pm 4\text{ mA}$. In other words, the nonreciprocal nonlocal spin transport is greatly suppressed in the region far away from the source and drain.

From the above observations, we find that (1) nonlocal spin signals exhibit the right-handed spin-momentum locking property, (2) the nonlocal spin voltage amplitude demonstrates a nonreciprocity with respect to the current direction at the high current bias, (3) the nonreciprocity is enhanced as the Fermi level is tuned toward the Dirac point, (4) the nonreciprocity is spatially dependent and mainly takes place near the source-drain leads. Next, we would like to discuss the possible mechanisms for these observations.

The right-handed spin-momentum locking measured at two sides of the nanoplate indicates the dominance of topological surface states in the nonlocal spin transport (see Appendix F). Since the spin polarization signals are mainly induced by nonlocal current flow, it is natural to attribute the nonreciprocal nonlocal spin signals to the asymmetric current amplitude when reversing the bias direction. This is expected when considering the asymmetric electrode geometry and inversion symmetry broken lattice structure [45–48]. However,

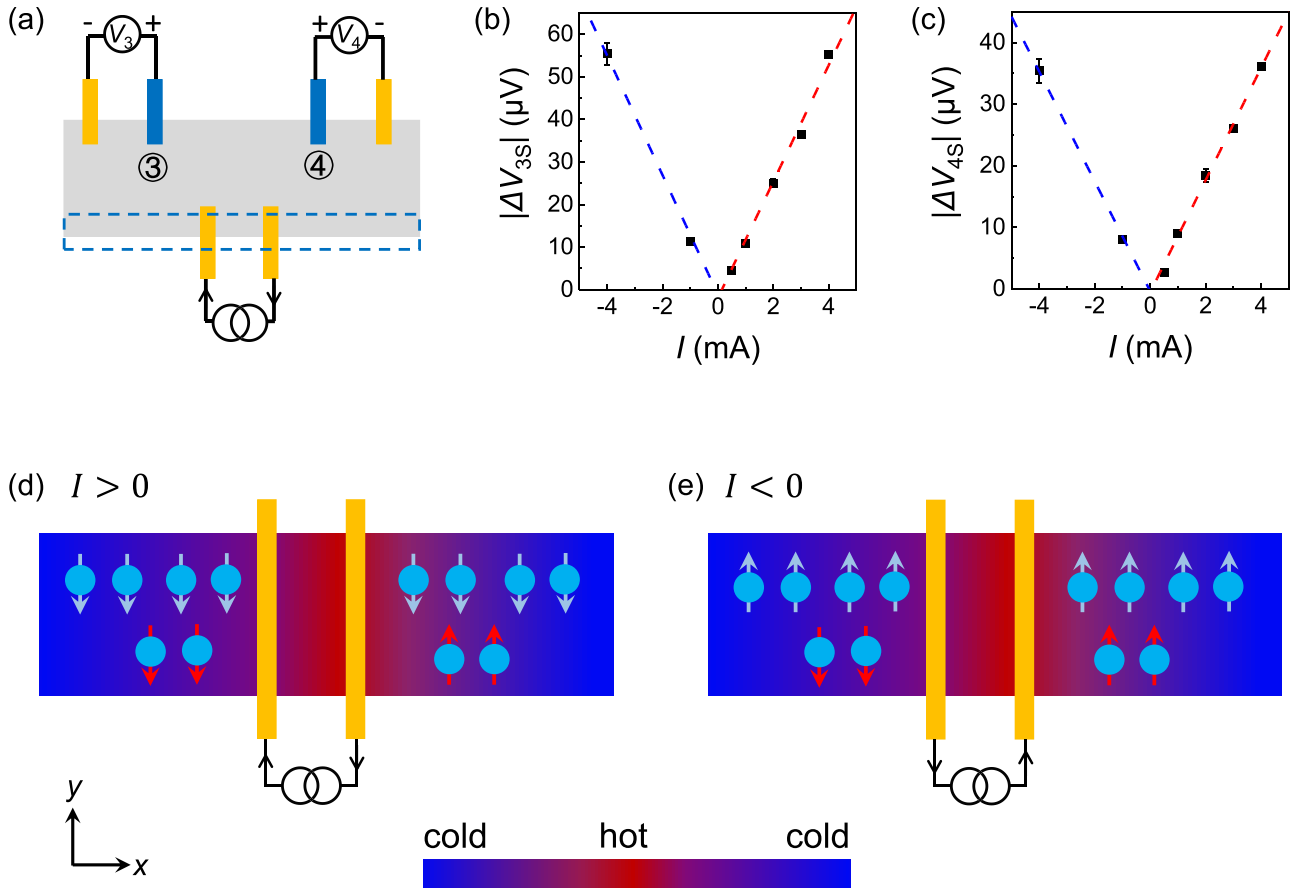


FIG. 4. Nonlocal spin transport measured in the regions far away from the source-drain leads. (a) Schematic of nonlocal measurement. The voltage measured on the Co electrodes 3 and 4 are denoted by V_3 and V_4 , respectively. The Co electrodes 3 and 4 are farther away from the source and drain compared to the Co electrodes 1 and 2. (b,c) The $|\Delta V_{3S}|$ and $|\Delta V_{4S}|$ as a function of bias current I in device B, which has almost the same electrode configuration as device A. The $|\Delta V_S|$ is almost equivalent for the same amplitude of positive and negative bias. Dashed blue and red lines are linear fits to experimental data at negative and positive currents, respectively. The error bars represent the standard deviation over multiple measurements. (d,e) Illustration of both current spreading induced surface spin polarization (gray arrows) and thermally induced surface spin polarization (red arrows) in the region near the current leads [highlighted by the dashed rectangle in (a)]. The filled blue circles represent the electrons, and the gray and red arrows denote the direction of electron spin.

as shown in Figs. 1(d) and 6, at low bias currents (where the Joule heating can be neglected), the nonlocal voltage shows a linear dependence on the bias current and an antisymmetric relationship as the current polarity is reversed. Therefore, the asymmetric current flow can be excluded as the main origin of nonreciprocal spin signals. Generally, spin diffusion of topological surface states from a local to a nonlocal region is also directional due to the spin-momentum locking. Nevertheless, the asymmetry of spin diffusion cannot explain the almost symmetric nonlocal spin transport at low bias current or in the region far away from the source-drain bias.

The enhanced nonreciprocity at higher bias, that is, the asymmetric spin signals, can be attributed to the thermal effect. Upon applying a high bias current (e.g., 2 mA), Joule heating would result in a temperature gradient ∇T between the source-drain region and its outside regions [49–51]. Moreover, the ∇T is almost the same for positive and negative current since it is proportional to I^2 . The ∇T will drive the carrier moving from the hot side to the cold side, and there will be notable spin accumulations due to spin-momentum locking of the topological surface states, which are independent of the

direction of source-drain current. By contrast, changing the bias current polarity, i.e., reversing the spreading current direction, results in opposite spin polarizations on the nanoplate surface due to the spin-momentum locking property of the topological surface states. Taking both the current spreading and thermally induced spin accumulations into consideration, it is expected to observe asymmetric nonlocal spin signals upon changing the bias current direction, as illustrated in Figs. 4(d) and 4(e).

The proposed thermal effect can also explain the gate-dependent nonreciprocity shown in Fig. 3. Since Joule heating power is proportional to electrical resistance at a fixed bias current, the thermal effect would be enhanced as the Fermi level is tuned toward the Dirac point to increase the resistance. This enhancement of thermal effect would enhance the nonreciprocity of nonlocal spin transport. Moreover, the Joule heating is mainly concentrated within and near the current leads. This is consistent with the experimental observation that nonreciprocity is pronounced near the source and drain while it is greatly reduced in the far region (see Appendix G).

IV. CONCLUSIONS

In summary, we have demonstrated the nonreciprocity of nonlocal spin transport relative to the direction of source-drain current in Dirac semimetal Cd₃As₂ nanoplates. It is found that, under a high current bias, Joule heating has significant influence on the nonlocal spin-polarized transport of topological surface states. The nonreciprocity is remarkable near the current leads and enhanced when the Fermi level is tuned close to the Dirac point. Our work exhibits gate tunable spin flow by means of the thermal effect, paving the way for developing thermospintronics [52–58] based on topological materials.

ACKNOWLEDGMENTS

This work was supported by the Innovation Program for Quantum Science and Technology (Grant No. 2021ZD0302403), the National Natural Science Foundation of China (Grants No. 91964201, No. 61825401, and No. 12204016) and the China Postdoctoral Science Foundation (Grant No. 2021M700254).

A.-Q.W. and P.-Z.X. contributed equally to this work.

APPENDIX A: CARRIER DENSITY OF THE SAMPLES

The transfer curve of device A, the longitudinal conductance G versus gate voltage V_g , is shown in Fig. 5(a). The gate voltage is applied onto the Si substrate with an oxide layer on top. We can obtain the carrier mobility μ by the linear fitting of conductance through $\mu = \frac{\partial G}{\partial V_g} \frac{1D_{ox}}{w\epsilon_0\epsilon_{ox}}$, where l , D_{ox} , w , ϵ_0 , and ϵ_{ox} denote the channel length, the thickness of the oxide layer, the sample width, the vacuum dielectric constant, and the dielectric constant of the oxide layer, respectively [17,59]. The linear fitting of the transfer curve gives $\frac{\partial G}{\partial V_g} = 2.2 \times 10^{-3} \Omega^{-1} \text{V}^{-1}$, as shown by the red curve in Fig. 5. Then the carrier density can be estimated as $n = \frac{\sigma}{e\mu}$ with the conductivity $\sigma = \frac{l}{wtR}$, where e , t , and R are electron charge, sample thickness, and resistance, respectively. Last, we can obtain $n = 1/(\frac{\partial G}{\partial V_g} \frac{D_{ox}}{\epsilon_0\epsilon_{ox}} eRt)$. At zero gate voltage, the measured resistance $R = 4.8 \Omega$ for the nanoplate with thickness $t \sim 100$ nm. Combined with the empirical value of D_{ox} , ϵ_0 , and ϵ_{ox} [17], the carrier density can be estimated as $n \sim 7.2 \times 10^{17} \text{cm}^{-3}$. The Fermi wave vector then is obtained as $k_F = (3\pi^2 n)^{1/3} \sim 0.028 \text{\AA}^{-1}$. The corresponding Fermi level $E_F = \hbar v_F k_F$ is about 91 meV using the Fermi velocity

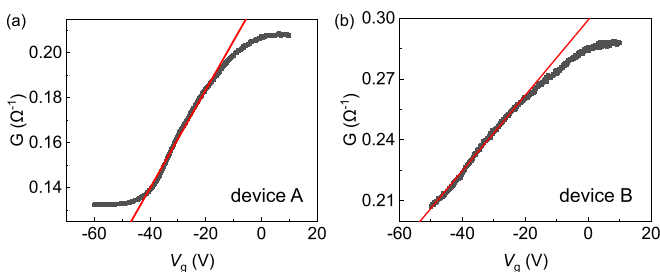


FIG. 5. Transfer curve of device A and device B. The conductance G as a function of gate voltage V_g . The red lines show the linear fitting of conductance, from which the carrier mobility and density can be obtained.

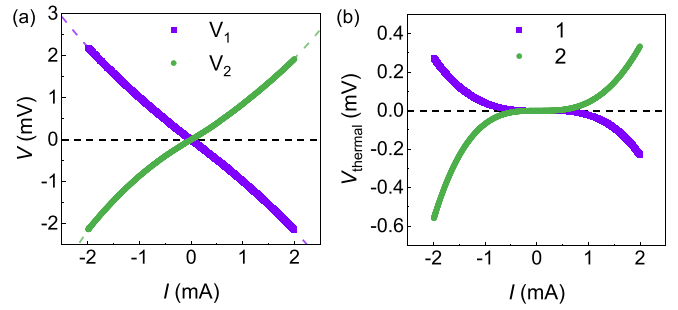


FIG. 6. Polynomial fitting of nonlocal I - V data and the estimated thermal voltage for device A. Four-degree polynomial fittings for the nonlocal V_1 and V_2 data of Fig. 1(d). (a) Higher-degree polynomials can always fit the data better, but the same linear components are still recognized. (b) The estimated thermal voltage $V_{\text{thermal}} \approx A_2 I^2 + A_3 I^3 + A_4 I^4$, where A_2 , A_3 , and A_4 are obtained from the fitting results in (a).

$v_F = 5 \times 10^5$ m/s. Similarly, we can obtain the carrier density $n \sim 1.2 \times 10^{18} \text{cm}^{-3}$ and $E_F \sim 107$ meV for device B [Fig. 5(b)]. Compared with the previous works on Cd₃As₂ nanoplates [14,15,17], the carrier density and Fermi level of the two devices are low enough to anticipate the observation of topological surface state spin transport.

APPENDIX B: ESTIMATION OF THERMALLY INDUCED VOLTAGE

To clarify the thermal effect on the nonlocal voltage, we fit the I - V data by high-degree polynomials [Fig. 6(a)]. The nonlocal voltage V can be expanded as $V = A_0 + A_1 I + A_2 I^2 + A_3 I^3 + \dots$. The term A_0 should be zero due to vanishing V in the absence of bias currents. The term A_1 is mainly caused by the Joule-Seebeck effect [40]. The higher-order components may come from other factors such as the temperature-dependent Seebeck coefficient [60]. Figure 6(a) shows the four-degree polynomial fitting results of nonlocal I - V data of Fig. 1(d). The thermoelectric effect generated voltage is estimated by the nonlinear terms, as displayed in Fig. 6(b). As expected, the thermoelectric voltage is almost negligible at low bias currents, and becomes gradually significant when $|I| > 0.5$ mA.

APPENDIX C: RAW DATA OF MAGNETIC HYSTERETIC LOOPS

Since bulk states also contribute to the nonlocal transport, the measured nonlocal voltages contain not only the spin-dependent signals, but also a spin-independent background. Figure 7 shows the raw data of magnetic hysteric loops measured on the Co electrode 1 of device A and electrode 4 of device B. A linear magnetoresistance background is clearly observed (dashed lines), which is consistent with previous observations [17]. The spin-dependent voltage V_S in the main text is obtained by subtracting the background signals from raw data.

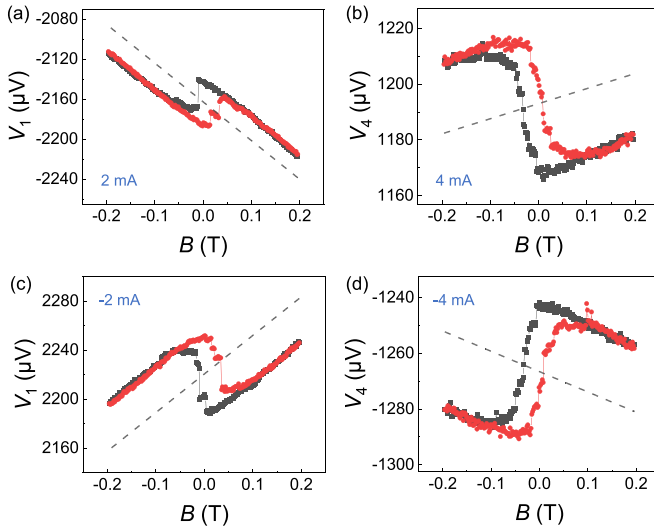


FIG. 7. Raw data of nonlocal spin transport measurements. (a,c) Raw data of nonlocal spin transport measured on the Co electrode 1 of device A (lower side of nanoplate), corresponding to Figs. 2(a) and 2(c) in the main text. (b,d) Raw data of nonlocal spin transport measured on the Co electrode 4 of device B (upper side of nanoplate). The linear magnetoresistance background is denoted by dashed lines.

APPENDIX D: GATE VOLTAGE DEPENDENCE OF ΔV_S

Figure 8 compares the magnetic hysteric loops under different gate voltages in device A. When the gate voltage is reduced from 0 to -60 V, the height of the hysteric window, i.e., the spin voltage amplitude $|\Delta V_S|$, experiences an obvious increase regardless of the direction of bias current. Meanwhile, the amplitude of the background signal is also enhanced. These observations are consistent with previous

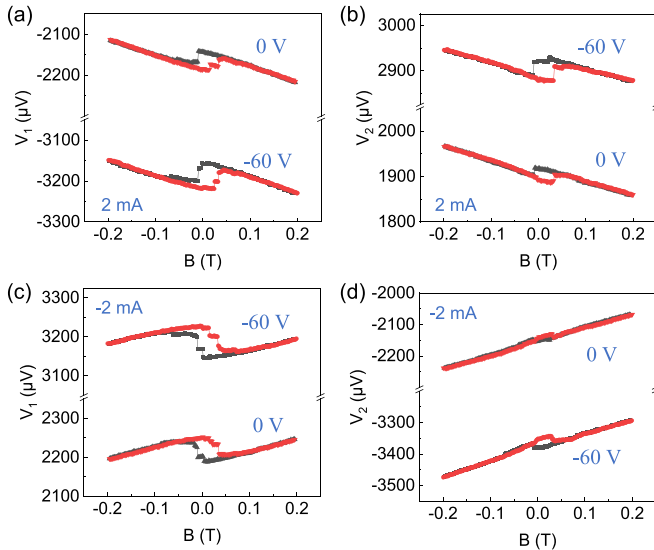


FIG. 8. Comparison of magnetic hysteric loops under different gate voltages in device A. (a,c) Raw data of nonlocal spin transport measured on the Co electrode 1 at $V_g = 0$ V and $V_g = -60$ V. (b,d) Raw data of nonlocal spin transport measured on the Co electrode 2 at $V_g = 0$ V and $V_g = -60$ V.

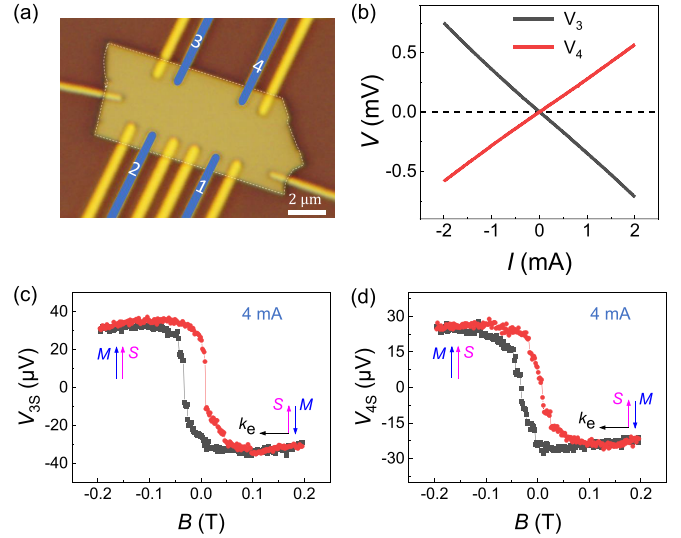


FIG. 9. Nonlocal spin transport measurements on the Co electrodes 3 and 4 in device B. (a) Optical image of the nanoplate device B. The Ti/Au and Co electrodes are marked by yellow and blue, respectively. (b) Nonlocal I - V characteristics measured on the Co electrodes 3 and 4 when the magnetic field $B = 0$ T. (c,d) Spin voltage loops measured on the Co electrodes 3 and 4 with a bias current of 4 mA.

results on a Cd_3As_2 nanoplate [15,17]. The $|\Delta V_S|$ is mainly originated from helical surface states (see Appendix F), and its amplitude is proportional to the charge current flowing through the surface channel [15]. In the Dirac semimetal Cd_3As_2 , the bulk and surface states are always in parallel conduction. As the nanoplate Fermi level is tuned toward the Dirac point, the bulk to surface conductance ratio is decreased, leading to an increase of spin-polarized surface current and $|\Delta V_S|$. On the other hand, the reduced bulk carrier density near the Dirac point results in an enhancement of electrical resistance and a larger amplitude of background voltage.

APPENDIX E: NONLOCAL MEASUREMENTS IN THE REGION FAR AWAY FROM CURRENT LEADS IN DEVICE B

Figure 9 demonstrates the nonlocal transport results measured on the Co electrodes 3 and 4 in device B. Device B has nearly the same electrode geometry as device A [Fig. 9(a)]. A dc bias current is injected into the nanoplate via the two Ti/Au electrodes between Co electrodes 1 and 2, whereas the voltage is measured on the Co electrodes 3 and 4 situated far away from the source-drain region. Linear I - V curves are observed even at large bias currents [Fig. 9(b)], in sharp contrast to Fig. 1(d) in the main text. Spin voltage loops are also clearly observed on the Co electrodes 3 and 4 [Figs. 9(c) and 9(d)]. With the determined orientations of momentum and spin, the right-handed spin-momentum locking relation can be obtained, which is consistent with the scenario of topological surface state spin transport.

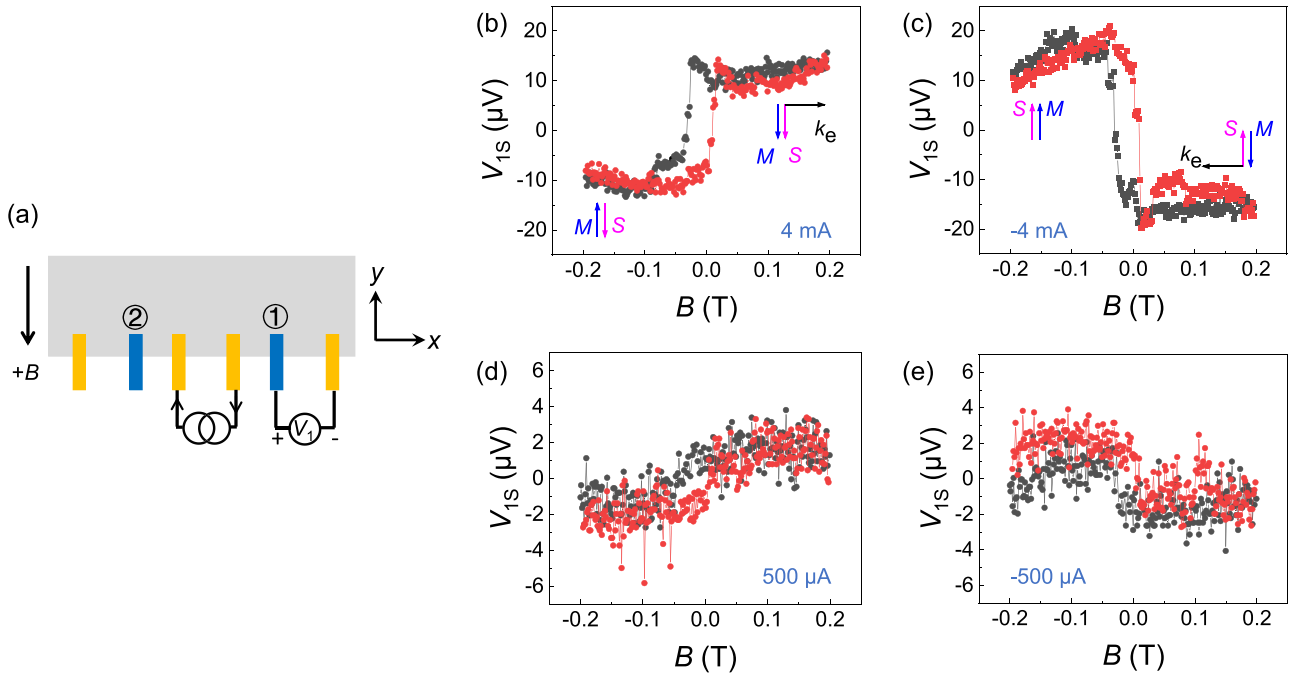


FIG. 10. Nonreciprocal nonlocal spin signals measured on the neighboring region to the current leads in device B. (a) Schematic illustration of nonlocal measurement geometry. The nonlocal voltage measured on the Co electrode 1 is denoted by V_1 . The positive current is applied along the $+x$ direction, and the positive magnetic field is applied along the $-y$ direction. (b,c) Nonlocal spin voltage V_{1S} loops measured on the Co electrode 1 with bias current ± 4 mA. (d,e) Nonlocal spin voltage V_{1S} loops measured on the Co electrode 1 with bias current $\pm 500 \mu\text{A}$.

APPENDIX F: NONLOCAL SPIN TRANSPORT OF TOPOLOGICAL SURFACE STATES

In the Dirac semimetal Cd_3As_2 , both the topological surface states and hinge states can contribute to the nonlocal spin signals due to the intrinsic spin-momentum locking property. The observed right-handed spin-momentum locking at both sides of the nanoplate indicates the dominance of topological surface states in nonlocal spin transport. This is because the hinge states possess an opposite spin-momentum locking relation at two sides of the Cd_3As_2 nanoplate [61], inconsistent with the experimental observation, which could not be the main origin of nonlocal spin signals. Moreover, the observed opposite spin polarizations upon reversing bias currents is consistent with the scenario of nonlocal charge current spreading induced surface spin transport. This suggests that the nonlocal spreading current induced surface spin polarization is dominant over the other factors, such as thermally induced spin polarization and intrinsic spin diffusion process. This is different from the previous investigation on ZrTe_5 nanowires [51], where the thermal effect dominates the nonlocal spin polarization and the charge current spreading is almost negligible. The reasons for such difference may lie in the discrepancy of the topological nature of the two materials. The nonlocal spin transport in our work should arise from the Fermi arc states which are unique to Dirac semimetals. Notably, upon the reversal of bias currents, we here observe a reversal of spin polarization in nonlocal regions of the Cd_3As_2 nanoplate, which is also different from the case of Cd_3As_2 nanowires [14]. Compared to nanowires, the Cd_3As_2 nanoplates usually have a higher carrier mobility, a

higher electrical conductivity, and a longer mean free path [59,62–64]. The longer mean free path and higher conductivity of nanoplates facilitate the dominance of the current spreading effect in the nonlocal channel, as also evidenced by the almost linear relation between nonlocal voltage and electric current [Fig. 1(d)]. As for the nanowire device [14], the nonlocal cobalt electrode is 350 nm away from the local two electrodes, much beyond its electron mean free path (~ 80 nm). Additionally, the nanowire usually has a higher electrical resistance due to its larger resistivity and suppressed cross-section area, and this would produce a considerable amount of Joule heat even in the presence of a small bias current. Therefore, the nonlocal current spreading effect is almost negligible in nanowires, and carrier diffusion comes into prominence. The carrier diffusion may originate from the thermal drive due to Joule heating, where the spin polarization remains the same upon reversing the bias current [14].

APPENDIX G: NONLOCAL SPIN TRANSPORT IN THE NEIGHBORING REGION TO CURRENT LEADS IN DEVICE B

Figure 10 shows the nonlocal spin transport results measured on the neighboring region to the current leads in device B. Compared to the data of electrodes 3 and 4 [Figs. 4(b) and 4(c)], electrode 1 detects nonreciprocal spin signals upon switching the bias direction [Figs. 10(b) and 10(c)]. This is expected since electrode 1 is situated near the current leads, where the thermal effect is more predominant than the remote electrodes 3 and 4. A combination of thermal effect and spin-momentum locked surface states gives rise to the

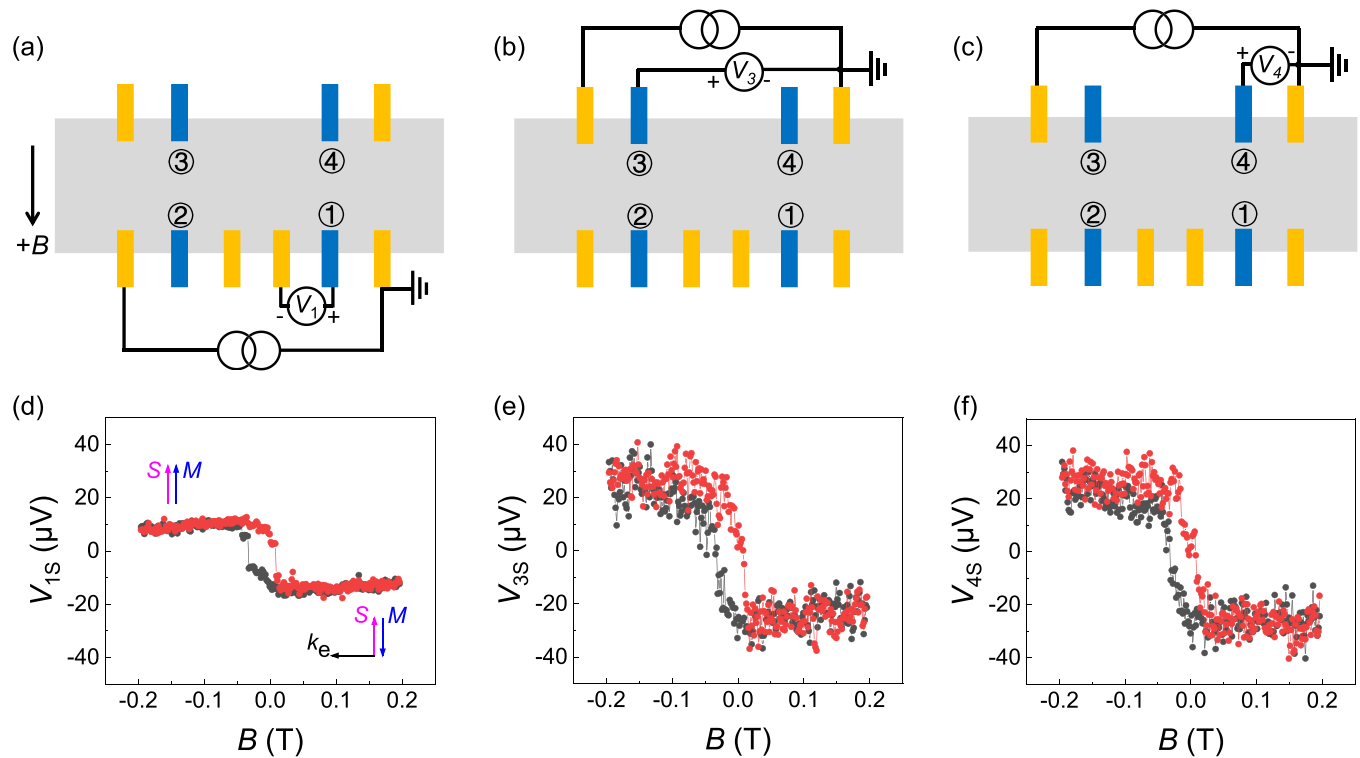


FIG. 11. Local spin transport measurements on the Co electrodes 1, 3, and 4 of device B. (a–c) Schematic illustration of local measurement geometry. The local voltage measured on the Co electrodes 1, 3, and 4 is denoted by V_1 , V_2 , and V_4 , respectively. (d–f) Local spin voltage V_S loops measured on the Co electrodes 1, 3, and 4 with bias current $300 \mu\text{A}$. The data in (d–f) are obtained from the measurement geometry (a–c), respectively.

observed nonreciprocity. As the bias current is decreased to a small value [Figs. 10(d) and 10(e)], the Joule heating is almost negligible and exerts little effect on the spin-polarized signals, where nonreciprocity would be greatly reduced upon reversing the current direction. In addition, we find the nonreciprocity in device B [Figs. 10(b) and 10(c)] is smaller than that in device A [Figs. 2(a) and 2(b)], although the bias current is much larger in device B. This is because the magnitude of nonreciprocity, i.e., the spin voltage asymmetry, depends on not only Joule heating term I^2R (the product of current square and device resistance), but also the thermal parameters of the nanoplate device, such as heat capacity, heat conductance, and Seebeck effect. The different carrier density [Fig. 5] would lead to a divergence of Seebeck coefficient and other thermal parameters between the two devices. Therefore, after considering other factors such as device resistance and Seebeck coefficient, it can be understandable that the nonreciprocity in device B is smaller than for device A, although the current

in device B (4 mA) is significantly larger than in device A (2 mA).

APPENDIX H: LOCAL SPIN TRANSPORT IN DEVICE B

Figure 11 shows the local spin detection on the Co electrodes 1, 3, and 4 of device B. In the presence of the same bias current ($I = 300 \mu\text{A}$), the Co electrodes 1, 3, and 4 exhibit different magnitudes of hysteresis window, i.e., different spin voltage amplitude $|\Delta V_S|$. As we can see, the $|\Delta V_S|$ is about $20 \mu\text{V}$ for Co electrode 1, while $|\Delta V_S|$ is about $60 \mu\text{V}$ for Co electrodes 3 and 4. On the same Cd_3As_2 nanoplate, the different $|\Delta V_S|/I$ indicates distinct interface quality and different spin detection efficiency of Co electrodes. Specifically, the efficiency of spin detection may be influenced by the roughness of the material surface, the crystal quality of the edge, the uniformity of the intermediate isolating layer, and the quality of the Co electrode.

- [1] X. Wan, A. M. Turner, A. Vishwanath, and S. Y. Savrasov, Topological semimetal and Fermi-arc surface states in the electronic structure of pyrochlore iridates, *Phys. Rev. B* **83**, 205101 (2011).
 [2] Z. Wang, Y. Sun, X.-Q. Chen, C. Franchini, G. Xu, H. Weng, X. Dai, and Z. Fang, Dirac semimetal and topological phase

- transitions in A_3Bi ($\text{A}=\text{Na}, \text{K}, \text{Rb}$), *Phys. Rev. B* **85**, 195320 (2012).
 [3] Z. Wang, H. Weng, Q. Wu, X. Dai, and Z. Fang, Three-dimensional Dirac semimetal and quantum transport in Cd_3As_2 , *Phys. Rev. B* **88**, 125427 (2013).

- [4] N. P. Armitage, E. J. Mele, and A. Vishwanath, Weyl and Dirac semimetals in three-dimensional solids, *Rev. Mod. Phys.* **90**, 015001 (2018).
- [5] A.-Q. Wang, X.-G. Ye, D.-P. Yu, and Z.-M. Liao, Topological semimetal nanostructures: From properties to topotronics, *ACS Nano* **14**, 3755 (2020).
- [6] D. Călugăru, V. Juričić, and B. Roy, Higher-order topological phases: A general principle of construction, *Phys. Rev. B* **99**, 041301(R) (2019).
- [7] M. Ezawa, Higher-Order Topological Insulators and Semimetals on the Breathing Kagome and Pyrochlore Lattices, *Phys. Rev. Lett.* **120**, 026801 (2018).
- [8] B. J. Wieder, Z. Wang, J. Cano, X. Dai, L. M. Schoop, B. Bradlyn, and B. A. Bernevig, Strong and fragile topological Dirac semimetals with higher-order Fermi arcs, *Nat. Commun.* **11**, 627 (2020).
- [9] C.-Z. Li, A.-Q. Wang, C. Li, W.-Z. Zheng, A. Brinkman, D.-P. Yu, and Z.-M. Liao, Reducing Electronic Transport Dimension to Topological Hinge States by Increasing Geometry Size of Dirac Semimetal Josephson Junctions, *Phys. Rev. Lett.* **124**, 156601 (2020).
- [10] S.-Y. Xu, C. Liu, S. K. Kushwaha, R. Sankar, J. W. Krizan, I. Belopolski, M. Neupane, G. Bian, N. Alidoust, T.-R. Chang *et al.*, Observation of Fermi arc surface states in a topological metal, *Science* **347**, 294 (2015).
- [11] B. Q. Lv, S. Muff, T. Qian, Z. D. Song, S. M. Nie, N. Xu, P. Richard, C. E. Matt, N. C. Plumb, L. X. Zhao *et al.*, Observation of Fermi-Arc Spin Texture in TaAs, *Phys. Rev. Lett.* **115**, 217601 (2015).
- [12] S.-Y. Xu, I. Belopolski, D. S. Sanchez, M. Neupane, G. Chang, K. Yaji, Z. Yuan, C. Zhang, K. Kuroda, G. Bian *et al.*, Spin Polarization and Texture of the Fermi Arcs in the Weyl Fermion Semimetal TaAs, *Phys. Rev. Lett.* **116**, 096801 (2016).
- [13] B. Feng, Y.-H. Chan, Y. Feng, R.-Y. Liu, M.-Y. Chou, K. Kuroda, K. Yaji, A. Harasawa, P. Moras, A. Barinov *et al.*, Spin texture in type-II Weyl semimetal WTe₂, *Phys. Rev. B* **94**, 195134 (2016).
- [14] B.-C. Lin, S. Wang, A.-Q. Wang, Y. Li, R.-R. Li, K. Xia, D. Yu, and Z.-M. Liao, Electric Control of Fermi Arc Spin Transport in Individual Topological Semimetal Nanowires, *Phys. Rev. Lett.* **124**, 116802 (2020).
- [15] A.-Q. Wang, P.-Z. Xiang, X.-G. Ye, W.-Z. Zheng, D. Yu, and Z.-M. Liao, Room-Temperature Manipulation of Spin Texture in a Dirac Semimetal, *Phys. Rev. Appl.* **14**, 054044 (2020).
- [16] I. Žutić, J. Fabian, and S. D. Sarma, Spintronics: Fundamentals and applications, *Rev. Mod. Phys.* **76**, 323 (2004).
- [17] A.-Q. Wang, P.-Z. Xiang, X.-G. Ye, W.-Z. Zheng, D. Yu, and Z.-M. Liao, Surface engineering of antisymmetric linear magnetoresistance and spin-polarized surface state transport in Dirac semimetals, *Nano Lett.* **21**, 2026 (2021).
- [18] W. Yanez, Y. Ou, R. Xiao, J. Koo, J. T. Held, S. Ghosh, J. Rabble, T. Pillsbury, E. G. Delgado, K. Yang *et al.*, Spin and Charge Interconversion in Dirac-Semimetal Thin Films, *Phys. Rev. Appl.* **16**, 054031 (2021).
- [19] P. Li, W. Wu, Y. Wen, C. Zhang, J. Zhang, S. Zhang, Z. Yu, S. A. Yang, A. Manchon, and X.-x. Zhang, Spin-momentum locking and spin-orbit torques in magnetic nano-heterojunctions composed of Weyl semimetal WTe₂, *Nat. Commun.* **9**, 3990 (2018).
- [20] D. MacNeill, G. M. Stiehl, M. H. D. Guimaraes, R. A. Buhrman, J. Park, and D. C. Ralph, Control of spin-orbit torques through crystal symmetry in WTe₂/ferromagnet bilayers, *Nat. Phys.* **13**, 300 (2017).
- [21] S. Shi, S. Liang, Z. Zhu, K. Cai, S. D. Pollard, Y. Wang, J. Wang, Q. Wang, P. He, J. Yu *et al.*, All-electric magnetization switching and Dzyaloshinskii-Moriya interaction in WTe₂/ferromagnet heterostructures, *Nat. Nanotechnol.* **14**, 945 (2019).
- [22] B. Zhao, B. Karpiak, D. Khokhriakov, A. Johansson, A. M. Hoque, X. Xu, Y. Jiang, I. Mertig, and S. P. Dash, Unconventional charge-spin conversion in Weyl-semimetal WTe₂, *Adv. Mater.* **32**, 2000818 (2020).
- [23] X.-G. Ye, P.-F. Zhu, W.-Z. Xu, N. Shang, K. Liu, and Z.-M. Liao, Orbit-transfer torque driven field-free switching of perpendicular magnetization, *Chin. Phys. Lett.* **39**, 037303 (2022).
- [24] J. Sinova, S. O. Valenzuela, J. Wunderlich, C. H. Back, and T. Jungwirth, Spin Hall effects, *Rev. Mod. Phys.* **87**, 1213 (2015).
- [25] J. Tian, C. Şahin, I. Miotkowski, M. E. Flatté, and Y. P. Chen, Opposite current-induced spin polarizations in bulk-metallic Bi₂Se₃ and bulk-insulating Bi₂Te₂Se topological insulator thin flakes, *Phys. Rev. B* **103**, 035412 (2021).
- [26] F. Yang, S. Ghatak, A. A. Taskin, K. Segawa, Y. Ando, M. Shiraishi, Y. Kanai, K. Matsumoto, A. Rosch, and Y. Ando, Switching of charge-current-induced spin polarization in the topological insulator BiSbTeSe₂, *Phys. Rev. B* **94**, 075304 (2016).
- [27] P. L. McEuen, A. Szafer, C. A. Richter, B. W. Alphenaar, J. K. Jain, A. D. Stone, R. G. Wheeler, and R. N. Sacks, New Resistivity for High-Mobility Quantum Hall Conductors, *Phys. Rev. Lett.* **64**, 2062 (1990).
- [28] A. Roth, C. Brüne, H. Buhmann, L. W. Molenkamp, J. Maciejko, X.-L. Qi, and S.-C. Zhang, Nonlocal transport in the quantum spin Hall state, *Science* **325**, 294 (2009).
- [29] L. Veyrat, C. Déprez, A. Coissard, X. Li, F. Gay, K. Watanabe, T. Taniguchi, Z. Han, B. A. Piot, H. Sellier *et al.*, Helical quantum Hall phase in graphene on SrTiO₃, *Science* **367**, 781 (2020).
- [30] P. Tiwari, S. K. Srivastav, S. Ray, T. Das, and A. Bid, Observation of time-reversal invariant helical edge-modes in bilayer graphene/WSe₂ heterostructure, *ACS Nano* **15**, 916 (2021).
- [31] D. J. Kim, S. Thomas, T. Grant, J. Botimer, Z. Fisk, and J. Xia, Surface Hall effect and nonlocal transport in SmB₆: Evidence for surface conduction, *Sci. Rep.* **3**, 3150 (2013).
- [32] M. Johnson and R. H. Silsbee, Calculation of nonlocal baseline resistance in a quasi-one-dimensional wire, *Phys. Rev. B* **76**, 153107 (2007).
- [33] A. Aharon-Steinberg, A. Marguerite, D. J. Perello, K. Bagani, T. Holder, Y. Myasoedov, L. S. Levitov, A. K. Geim, and E. Zeldov, Long-range nontopological edge currents in charge-neutral graphene, *Nature (London)* **593**, 528 (2021).
- [34] S. Wolgast, Ç. Kurdak, K. Sun, J. W. Allen, D.-J. Kim, and Z. Fisk, Low-temperature surface conduction in the Kondo insulator SmB₆, *Phys. Rev. B* **88**, 180405(R) (2013).
- [35] C. Shekhar, C. E. ViolBarbosa, B. Yan, S. Ouardi, W. Schnelle, G. H. Fecher, and C. Felser, Evidence of surface transport and weak antilocalization in a single crystal of the Bi₂Te₂Se topological insulator, *Phys. Rev. B* **90**, 165140 (2014).
- [36] J. Lee, J.-H. Lee, J. Park, J. S. Kim, and H.-J. Lee, Evidence of Distributed Robust Surface Current Flow in 3D Topological Insulators, *Phys. Rev. X* **4**, 011039 (2014).

- [37] T.-H. Hwang, H.-S. Kim, H. Kim, J. S. Kim, and Y.-J. Doh, Electrical detection of spin-polarized current in topological insulator $\text{Bi}_{1.5}\text{Sb}_{0.5}\text{Te}_{1.7}\text{Se}_{1.3}$, *Curr. Appl. Phys.* **19**, 917 (2019).
- [38] S. Hong, V. Diep, S. Datta, and Y. P. Chen, Modeling potentiometric measurements in topological insulators including parallel channels, *Phys. Rev. B* **86**, 085131 (2012).
- [39] C. Mu, S. Hu, J. Wang, and T. Kimura, Thermo-electric effect in a nano-sized crossed Permalloy/Cu junction under high bias current, *Appl. Phys. Lett.* **103**, 132408 (2013).
- [40] J. Hu, G. Stecklein, D. A. Deen, Q. Su, P. A. Crowell, and S. J. Koester, Scaling of the nonlocal spin and baseline resistances in graphene lateral spin valves, *IEEE Trans. Electron Devices* **66**, 5003 (2019).
- [41] A. Dankert, J. Geurs, M. V. Kamalakar, S. Charpentier, and S. P. Dash, Room temperature electrical detection of spin polarized currents in topological insulators, *Nano Lett.* **15**, 7976 (2015).
- [42] J. Tang, L.-T. Chang, X. Kou, K. Murata, E. S. Choi, M. Lang, Y. Fan, Y. Jiang, M. Montazeri, W. Jiang *et al.*, Electrical detection of spin-polarized surface states conduction in $(\text{Bi}_{0.53}\text{Sb}_{0.47})_2\text{Te}_3$ topological insulator, *Nano Lett.* **14**, 5423 (2014).
- [43] J. Tian, I. Miotkowski, S. Hong, and Y. P. Chen, Electrical injection and detection of spin-polarized currents in topological insulator $\text{Bi}_2\text{Te}_2\text{Se}$, *Sci. Rep.* **5**, 14293 (2015).
- [44] Y. Ando, T. Hamasaki, T. Kurokawa, K. Ichiba, F. Yang, M. Novak, S. Sasaki, K. Segawa, Y. Ando, and M. Shiraishi, Electrical detection of the spin polarization due to charge flow in the surface state of the topological insulator $\text{Bi}_{1.5}\text{Sb}_{0.5}\text{Te}_{1.7}\text{Se}_{1.3}$, *Nano Lett.* **14**, 6226 (2014).
- [45] T. Ideue, K. Hamamoto, S. Koshikawa, M. Ezawa, S. Shimizu, Y. Kaneko, Y. Tokura, N. Nagaosa, and Y. Iwasa, Bulk rectification effect in a polar semiconductor, *Nat. Phys.* **13**, 578 (2017).
- [46] R. Wakatsuki, Y. Saito, S. Hoshino, M. Itahashi Yuki, T. Ideue, M. Ezawa, Y. Iwasa, and N. Nagaosa, Nonreciprocal charge transport in noncentrosymmetric superconductors, *Sci. Adv.* **3**, e1602390 (2017).
- [47] R. Wakatsuki and N. Nagaosa, Nonreciprocal Current in Noncentrosymmetric Rashba Superconductors, *Phys. Rev. Lett.* **121**, 026601 (2018).
- [48] K. Yasuda, H. Yasuda, T. Liang, R. Yoshimi, A. Tsukazaki, K. S. Takahashi, N. Nagaosa, M. Kawasaki, and Y. Tokura, Nonreciprocal charge transport at topological insulator/superconductor interface, *Nat. Commun.* **10**, 2734 (2019).
- [49] A. Yamaguchi, S. Nasu, H. Tanigawa, T. Ono, K. Miyake, K. Mibu, and T. Shinjo, Effect of Joule heating in current-driven domain wall motion, *Appl. Phys. Lett.* **86**, 012511 (2005).
- [50] H. Tohmyoh, T. Imaizumi, H. Hayashi, and M. Saka, Welding of Pt nanowires by Joule heating, *Scr. Mater.* **57**, 953 (2007).
- [51] J. Ning, W. Peng, W. Wang, Z. Chen, P. Yang, Y. Chen, Y. Zhao, Y. Sun, M. Kanagaraj, L. Yang *et al.*, Thermal induced spin-polarized current protected by spin-momentum locking in ZrTe_5 nanowires, *Phys. Rev. B* **104**, 035429 (2021).
- [52] K. Uchida, S. Takahashi, K. Harii, J. Ieda, W. Koshibae, K. Ando, S. Maekawa, and E. Saitoh, Observation of the spin Seebeck effect, *Nature (London)* **455**, 778 (2008).
- [53] C. M. Jaworski, R. C. Myers, E. Johnston-Halperin, and J. P. Heremans, Giant spin Seebeck effect in a non-magnetic material, *Nature (London)* **487**, 210 (2012).
- [54] T. T. Heikkilä and Y. Tserkovnyak, Thermal spin power without magnets, *Nature (London)* **487**, 180 (2012).
- [55] A. Slachter, F. L. Bakker, J. P. Adam, and B. J. van Wees, Thermally driven spin injection from a ferromagnet into a non-magnetic metal, *Nat. Phys.* **6**, 879 (2010).
- [56] J.-C. Le Breton, S. Sharma, H. Saito, S. Yuasa, and R. Jansen, Thermal spin current from a ferromagnet to silicon by Seebeck spin tunnelling, *Nature (London)* **475**, 82 (2011).
- [57] T. Kimura, T. Sato, and Y. Otani, Temperature Evolution of Spin Relaxation in a NiFe/Cu Lateral Spin Valve, *Phys. Rev. Lett.* **100**, 066602 (2008).
- [58] M. Hatami, G. E. W. Bauer, Q. Zhang, and P. J. Kelly, Thermal Spin-Transfer Torque in Magnetoelectronic Devices, *Phys. Rev. Lett.* **99**, 066603 (2007).
- [59] C.-Z. Li, J.-G. Li, L.-X. Wang, L. Zhang, J.-M. Zhang, D. Yu, and Z.-M. Liao, Two-carrier transport induced hall anomaly and large tunable magnetoresistance in dirac semimetal Cd_3As_2 Nanoplates, *ACS Nano* **10**, 6020 (2016).
- [60] F. L. Bakker, A. Slachter, J. P. Adam, and B. J. van Wees, Interplay of Peltier and Seebeck Effects in Nanoscale Nonlocal Spin Valves, *Phys. Rev. Lett.* **105**, 136601 (2010).
- [61] A.-Q. Wang, P.-Z. Xiang, T.-Y. Zhao, and Z.-M. Liao, Topological nature of higher-order hinge states revealed by spin transport, *Sci. Bull.* **67**, 788 (2022).
- [62] T. Liang, Q. Gibson, M. N. Ali, M. Liu, R. J. Cava, and N. P. Ong, Ultrahigh mobility and giant magnetoresistance in the Dirac semimetal Cd_3As_2 , *Nat. Mater.* **14**, 280 (2015).
- [63] C. Z. Li, L. X. Wang, H. Liu, J. Wang, Z. M. Liao, and D. P. Yu, Giant negative magnetoresistance induced by the chiral anomaly in individual Cd_3As_2 nanowires, *Nat. Commun.* **6**, 10137 (2015).
- [64] H. Pan, K. Zhang, Z. Wei, B. Zhao, J. Wang, M. Gao, L. Pi, M. Han, F. Song, X. Wang *et al.*, Quantum oscillation and nontrivial transport in the Dirac semimetal Cd_3As_2 nanodevice, *Appl. Phys. Lett.* **108**, 183103 (2016).